

State-estimation approach to the nonstationary optical tomography problem

Ville Kolehmainen

Department of Applied Physics, University of Kuopio, P.O. Box 1627, FIN-70211 Kuopio, Finland

Simon Prince

Department of Electrical and Computer Engineering, National University of Singapore, 4 Engineering Drive 3, Singapore 113576

Simon R. Arridge

Department of Computer Science, University College London, Gower Street, London, WC1E 6BT, UK

Jari P. Kaipio

Department of Applied Physics, University of Kuopio, P.O. Box 1627, FIN-70211 Kuopio, Finland

Received June 28, 2002; revised manuscript received December 3, 2002; accepted December 4, 2002

We propose a new numerical approach to the nonstationary optical (diffusion) tomography (OT) problem. The assumption in the method is that the absorption and/or diffusion coefficients are nonstationary in the sense that they may exhibit significant changes during the time that is needed to measure data for one traditional image frame. In the proposed method, the OT problem is formulated as a state-estimation problem. Within the state-estimation formulation, the absorption and/or diffusion coefficients are considered a stochastic process. The objective is to estimate a sequence of states for the process when the state evolution model for the process, the observation model for OT experiments, and data on the exterior boundary are given. In the proposed method, the state estimates are computed by using Kalman filtering techniques. The performance of the proposed method is evaluated on the basis of synthetic data. The simulations also illustrate that further improvements to the results in nonstationary applications can be obtained by adjustment of the measurement protocol. © 2003 Optical Society of America

OCIS codes: 100.3190, 170.3010, 170.6960.

1. INTRODUCTION

A. Optical Tomography

The concept of using optical radiation to penetrate highly scattering media, combined with image reconstruction methods to recover optical parameters inside the media, has been a recurrent idea for over a century^{1–3} but has received great attention in the last decade because of advances both in measurement technology and in theoretical and practical understanding of the nature of the image reconstruction problem. For recent reviews, see Refs. 4–10.

The major emphasis in the application of optical (diffusion) tomography (OT), which is a contributing factor to the growth in interest of the field, has been in medicine, where applications include detection and classification of tumors from breast tissue,^{11–13} monitoring of infant brain tissue oxygenation level,^{14–16} and functional brain activation studies.^{17–20} These applications are mainly based on the fact that absorption of near-infrared light in biological tissue depends on the oxygenation level of the tissue,^{21–23} thus providing valuable information about the physiological state of the tissue. In addition to medical applications, there has been recently a growing interest toward the use of optical methods in industrial process

tomography.²⁴ One possible application of OT in process tomography is monitoring of pulp mixture flows in pipelines in the paper industry.

B. Problem Description

In an OT experiment, S optic fibers are placed on the source positions $\varepsilon_k \subset \partial\Omega$ on the exterior boundary of a (highly scattering) body Ω , and M optic fibers are placed in the detector positions $\zeta_i \subset \partial\Omega$. Light from a near-infrared laser source is guided to the body by means of one of the source fibers at ε_k , and the amount of transmitted light is measured on all the detector locations ζ_i , $i = 1, \dots, M$, by using the detector fibers and light-sensitive detectors. This process is then repeated for all S source locations. This data set constitutes the data for one traditional image frame. Based on this set of transmission data on $\partial\Omega$, the objective is to estimate the absorption and/or diffusion coefficients within the body Ω . This estimation problem is a nonlinear ill-posed inverse boundary value problem.^{8,25–27}

All the reconstruction methods that have been proposed for the OT problem, such as the perturbation methods that are based on a first-order linear approximation of the problem (see, e.g., Refs. 28–32) or the methods that

are based on the regularized output least-squares (LS) formulation of the problem (see, e.g., Refs. 8, 25–27, and 33–35) are based on the (implicit) assumption that the absorption and diffusion coefficients are *stationary* in the sense that they do not change during the time that is needed to acquire data for one traditional image frame. This is also the case even in fast acquisition systems that attempt to reconstruct dynamic images on a time-frame-to-time-frame basis.^{36,37} However, in certain applications, such as functional brain activation studies, in which the goal is to track changes in spatial blood perfusion/oxygenation levels in the cortex due to some mental or physiological stimuli, the absorption and/or diffusion coefficients may vary significantly during the acquisition of one traditional image frame. To obtain feasible reconstructions in such a case, one should model the absorption and/or diffusion coefficients as time-varying (i.e., *nonstationary*) quantities.

C. State-Estimation Method

In this study, we propose a novel approach to the nonstationary OT problem, based on the state-estimation approach. In this framework, the absorption and/or diffusion coefficients are considered a multivariate stochastic process. The assumed temporal properties of this process are described in terms of a state evolution equation, and the observations on $\partial\Omega$, together with the measurement noise, are described in terms of an observation equation. Given this pair of equations and the data on $\partial\Omega$, the objective is to compute estimates for a sequence of states of the process.^{38–40}

The state-estimation approach to OT has previously been mentioned implicitly in Refs. 41 and 42, where the equivalent recursive linear filters were used to solve a stationary OT problem. However, we present here the first application of Kalman filtering to the dynamical OT problem. The rest of this paper is organized as follows. In Section 2, we discuss briefly the forward model that we use for the OT experiments. In Section 3, the OT inverse problem is formulated as a state-estimation problem, and the estimation of the states using the Kalman filtering techniques are discussed. In Section 4, the performance of the method is evaluated by using synthetic continuous-wave (cw) data. In the simulations, it is also illustrated that, in addition to a properly chosen inversion method, further improvements to results of the nonstationary OT problem can be obtained by adjustments of the data-acquisition protocol. In Section 5, we give conclusions and some suggestions for future work.

2. FORWARD MODEL

A. Diffusion Approximation to the Radiative Transfer Equation

Although the radiative transfer equation is a more appropriate mathematical model for the OT experiments, most of the current approaches to OT use the diffusion approximation (DA) to the radiative transfer equation as the mathematical model, which is also the model that we use in this paper. In the frequency domain, the DA assumes the form

$$-\nabla \cdot \kappa(r) \nabla \Phi_k(r, \omega) + \mu_a(r) \Phi_k(r, \omega) + \frac{i\omega}{c} \Phi_k(r, \omega) = q_{0,k}(r, \omega), \quad r \in \Omega, \quad (1)$$

where ω is the modulation frequency of the light source, $\Phi_k(r, \omega)$ is the photon density (for the source at $\varepsilon_k \subset \partial\Omega$), $\mu_a(r)$ is the absorption coefficient (mm^{-1}), $\kappa(r) = \{3[\mu_a(r) + \mu'_s(r)]\}^{-1}$ is the diffusion coefficient (mm), $\mu'_s(r)$ is the reduced scattering coefficient (mm^{-1}), c is the speed of light in the medium, and $q_{0,k}(r, \omega)$ is the distribution of internal light sources within Ω .⁸ For further details on the DA, see, e.g., Refs. 8, 43–46.

There are a variety of different boundary conditions that have been used with DA (see, e.g., Refs. 8 and 47–49). In this paper, we use the Robin-type boundary condition with the refractive-index mismatch between the body Ω and the surrounding medium. In the frequency domain, this condition assumes the form

$$\Phi_k(r, \omega) + 2\kappa(r)\theta \frac{\partial \Phi_k(r, \omega)}{\partial \hat{n}} = g_k(r, \omega), \quad r \in \partial\Omega, \quad (2)$$

where $g_k(r, \omega)$ is the distribution of boundary sources for the source at ε_k , \hat{n} is the boundary normal direction, and θ is a coefficient due to the mismatch of the refractive indices in the body Ω and the surrounding medium.⁴⁷

There are two commonly used source models for the DA, namely, the collimated source model and the diffuse boundary source model.^{8,47} In the collimated source model, the distribution of boundary sources is set to zero, that is, $g_k(r, \omega) \equiv 0$, and the light source is modeled as an isotropic point source located at depth $1/\mu'_s$ below the source site ε_k [i.e., the source becomes the internal source term $q_{0,k}(r, \omega)$]. In this study, we use the diffuse boundary source model, in which the source is modeled as an inward-directed diffuse photon current $\Gamma_s(r, \omega)$, which naturally becomes a part of the boundary condition (2). That is, we set $q_{0,k}(r, \omega) \equiv 0$, and $g_k(r, \omega)$ in Eq. (2) is of the form

$$g_k(r, \omega) = \begin{cases} -4\Gamma_s(r, \omega), & r \in \varepsilon_k \\ 0, & r \in \partial\Omega \setminus \varepsilon_k \end{cases}. \quad (3)$$

For further details on the source models, see Ref. 47. Results of earlier studies have shown that differences in these models are significant only within very small distances from the input position.⁴⁷ In the DA model, the measured flux $\Gamma_{i,k}(r, \omega)$ at the measurement site $\zeta_i \subset \partial\Omega$ for the k th source is obtained as^{8,43}

$$\Gamma_{i,k}(r, \omega) = -\kappa(r)\hat{n} \cdot \nabla \Phi_k(r, \omega), \quad r \in \zeta_i \subset \partial\Omega. \quad (4)$$

The DA has been validated to give reasonable accuracy in scattering-dominated media ($\mu'_s \gg \mu_a$) and when the point of interest is not very close to the light sources.^{8,50,51} In cases where these assumptions are not valid, alternative models have to be employed.^{46,52} A treatment of the performance of the state-space-estimation method under these conditions would also be possible but is outside the scope of the present paper.

B. Notation for the Forward Problem, the Parameter Vectors, and the Data

The forward problem in OT is to compute the data on $\partial\Omega$ when the absorption and diffusion coefficients and the distribution of the light sources on $\partial\Omega$ are given. In this study, the numerical solution of this boundary-value problem is based on the finite-element method (FEM). The FEM discretization of the problem [Eqs. (1)–(4)] has been presented in previous papers; for details see, e.g., Refs. 8, 43, 47, and 53. In the subsequent sections, we use the following notation for the FEM-based forward solver.

The discretizations of the coefficients (μ_a , κ) are expressed in the form

$$\mu_a(r) = \sum_{j=1}^{M_\mu} \mu_{a,j} \chi_j^{(\mu)}(r), \quad (5)$$

$$\kappa(r) = \sum_{j=1}^{M_\kappa} \kappa_j \chi_j^{(\kappa)}(r), \quad (6)$$

where the functions $\chi_j^{(\mu)}(r)$ and $\chi_j^{(\kappa)}(r)$ form the basis for the absorption and diffusion images (in this study, they are characteristic functions of disjoint pixels). Within expressions (5) and (6), we identify the discretization of the functions ($\mu_a(r)$, $\kappa(r)$) with the vectors

$$\mu_a = (\mu_{a,1}, \dots, \mu_{a,M_\mu})^T \in \mathbb{R}^{M_\mu}, \quad (7)$$

$$\kappa = (\kappa_1, \dots, \kappa_{M_\kappa})^T \in \mathbb{R}^{M_\kappa}. \quad (8)$$

There are a variety of different parameterizations that have been used for the inverse problem in OT.⁸ Especially if the continuous-wave (cw) data (i.e., modulation frequency $\omega = 0$) are employed, it is very typical that only the absorption coefficient μ_a is reconstructed, while diffusion is (implicitly) assumed to be a known quantity.⁵⁴ To simplify the notation, we denote the parameter vector for the inverse problem by f . In the case in which only absorption is reconstructed, we have $f = \mu_a \in \mathbb{R}^{M_\mu}$, and in the case in which both coefficients are reconstructed, we have

$$f = \begin{pmatrix} \mu_a \\ \kappa \end{pmatrix} \in \mathbb{R}^{M_\mu + M_\kappa}. \quad (9)$$

In this study, the data that are measured on all the detector locations ζ_i , $i = 1, 2, \dots, M$, for the source at ε_k are denoted by the vector

$$z^{(k)} = (z_{1,k}, \dots, z_{M,k})^T,$$

and the respective part of the forward map $F^{(k)}: f \mapsto z^{(k)}$ is denoted by

$$z^{(k)} = F^{(k)}(f). \quad (10)$$

Finally, for the data that correspond to one traditional image frame, we use the notation

$$z = \begin{pmatrix} z^{(1)} \\ \vdots \\ z^{(S)} \end{pmatrix}, \quad F(f) = \begin{pmatrix} F^{(1)}(f) \\ \vdots \\ F^{(S)}(f) \end{pmatrix}. \quad (11)$$

3. INVERSE PROBLEM

A. Stationary Case

Consider for a moment the OT problem in the case in which the coefficient vector f does not change during the acquisition of the data vector z in Eqs. (11). A typical (implicit) assumption in OT is that the observations are corrupted by additional zero-mean Gaussian random noise; i.e., the observation model assumes the form

$$z = F(f) + n, \quad (12)$$

where n denotes the noise vector.^{14,27} Under these assumptions, a traditional formulation of the inverse problem is to state the problem as an output LS problem:

$$\Xi(f) = \|z - F(f)\|^2. \quad (13)$$

However, because of the ill-posed nature of the OT problem, minimization of Eq. (13) necessitates regularization. One of the most commonly used approaches to regularization is (generalized) Tikhonov regularization; i.e., instead of minimizing the output LS functional, one considers the minimization of the regularized modification

$$\Xi(f) = \|z - F(f)\|^2 + \beta A(f), \quad (14)$$

where $\beta > 0$ is a regularization parameter that is used to control the relative weighting between the data residual norm and the regularizing penalty functional $A(f)$. In most cases, $A(f)$ is chosen to be of the form

$$A(f) = \|Rf\|^2, \quad (15)$$

where the matrix R is a properly chosen regularization operator. Loosely speaking, Eq. (14) can be interpreted such that the original LS problem is augmented with additional data that are based on *a priori* information or assumptions about the sought quantity f . For discussions on the different choices of the regularizing penalty functionals in OT, see, e.g., Refs. 27, 33, 34, 53, and 55.

B. Nonstationary Case

Consider the state-estimation approach to the nonstationary OT problem. The assumption is that f may vary significantly during the time that is needed to measure data for one traditional image frame. We assume that the problem has been discretized also with respect to the time variable. As general references to state estimation, see, e.g., Refs. 56–61. For previous papers on application of the state-estimation approach to large-dimensional ill-posed inverse problems, see Refs. 38, 39, and 62.

Within the discrete time framework, the parameters f are considered a multivariate real-valued stochastic process that has an evolution equation of the Markov type:

$$f_{t+1} = K_t f_t + w_t, \quad t \in \mathcal{I} = \{1, 2, \dots, T\},$$

$$w_t \sim \mathcal{N}(0, C_{w,t}), \quad (16)$$

where K_t is the state transition matrix, w_t denotes a zero-mean state noise process with a covariance matrix $\text{cov}(w_t) = C_{w,t}$, and the subindex t denotes the integer time steps. Matrix K_t represents the deterministic part of the state evolution model. It can be based on, e.g., physiological prior information on medical applications, or in process tomography applications it can be based on flow models.^{39,62} If there is no specific (deterministic) model available and f can be assumed to change slowly, a

typical choice for the state transition matrix is $K_t = I$, the identity matrix. With this choice, the evolution model for f becomes a random-walk model. We note here that “changing slowly” refers to changes between each individual time step, not to the time required to measure a traditional frame in OT.

For the relation between the parameters f and the data z_t that are measured on $\partial\Omega$ at time t , we write the additive noise model

$$z_t = F_t(f_t) + n_t, \quad n_t \sim \mathcal{N}(0, C_{n,t}), \quad (17)$$

where n_t denotes an observation noise process with a covariance matrix $\text{cov}(n_t) = C_{n,t}$. In Eq. (17), we assume that the parameter vector f is time invariant during the acquisition of the observations z_t . At this point, we do not specify further the observation vector z_t , except that in the most usual cases z_t would correspond to all measurements that are obtained simultaneously.

Equations (16) and (17) constitute the state-space representation of the OT problem. In the usual formulation of the state-estimation problem, the objective is to compute the conditional expectations

$$f_{t|\mathcal{I}_k} = E(f_t|z_k, k \in \mathcal{I}_k), \quad (18)$$

where $\mathcal{I}_k \subseteq \mathcal{I}$ is a subset of all measurements \mathcal{I} . Below, we will use the usual notation $f_{t|\mathcal{I}_k}$ for the estimate $f_{t|\mathcal{I}_k}$ with $\mathcal{I}_k = \{1, 2, \dots, k\}$. If $k < t$, $k = t$, or $k > t$, the problem of determining the estimate $f_{t|\mathcal{I}_k}$ is called prediction, filtering, or smoothing, respectively. In the case of linear evolution and observation equations, the Kalman filter algorithm can be used for determining the estimates $f_{t|t}$, $t \in \mathcal{I}$. However, in nonlinear problems the Kalman filter is not applicable, and determining the exact conditional expectations $f_{t|t}$ would be computationally infeasible.

Suboptimal estimates in nonlinear cases can be obtained by writing linear approximations for nonlinear evolution and/or observation equations and applying the Kalman filter algorithm to the linearized problem. This commonly used approach is called the extended Kalman filter. The linearized approximation for the observation equation (17) is written as

$$z_t = F_t(f_t^*) + J_t(f_t^*)(f_t - f_t^*) + n_t, \quad t \in \mathcal{I}, \quad (19)$$

where f_t^* is the linearization point in the state space and $F_t(f_t^*)$ and $J_t(f_t^*)$ are the parts of the forward solution and the Jacobian $J = \partial F(f)/\partial f$ that correspond to the data acquired at time t . The computation of the Jacobian has been presented in previous papers (see, e.g., Ref. 8).

Assuming that the noise processes w_t and n_t are Gaussian with zero mean and that the noise processes are orthogonal in the sense that $E(n_t n_{t+k}^T) = 0$, $E(w_t w_{t+k}^T) = 0 \forall k \neq 0$, and $E(n_t w_{t+k}^T) = 0 \forall k$, the approximations for the estimates $f_{t|t}$ can be obtained recursively by using the equations (with initializations $f_{1|0}$ and $C_{1|0}$)

$$G_t = C_{t|t-1} J_t^T(f_t^*) [J_t(f_t^*) C_{t|t-1} J_t^T(f_t^*) + C_{n,t}]^{-1}, \quad (20)$$

$$f_{t|t} = f_{t|t-1} + G_t [z_t - F_t(f_t^*) - J_t(f_t^*)(f_{t|t-1} - f_t^*)], \quad (21)$$

$$C_{t|t} = C_{t|t-1} - G_t J_t(f_t^*) C_{t|t-1}, \quad (22)$$

$$f_{t+1|t} = K_t f_{t|t}, \quad (23)$$

$$C_{t+1|t} = K_t C_{t|t} K_t^T + C_{w,t}, \quad (24)$$

where the matrix G_t is called the Kalman gain and the matrices $C_{t|t}$ and $C_{t+1|t}$ are the estimation error covariance matrices for the Kalman filter state vector $f_{t|t}$ and the predictor $f_{t+1|t}$, respectively. Each recursion of Eqs. (20)–(24) consists of two basic steps: (1) Equations (20)–(22) are used to update the state estimate and the estimation error covariance when the data z_t are obtained, and (2) Eqs. (23) and (24) are then used to extrapolate the state estimate and the estimation error covariance based on the state evolution model. The initial values $f_{1|0}$ and $C_{1|0}$ describe our knowledge of the first state f_1 before any observations.

Further, we note that if the observation model is linearized at the current value of the predictor, i.e., $f_t^* = f_{t|t-1}$, Eq. (21) assumes the form

$$f_{t|t} = f_{t|t-1} + G_t [z_t - F_t(f_{t|t-1})]. \quad (25)$$

It should be noted that the extended Kalman filter yields approximative results, and, in general, the accuracy of the estimates depends on how nonlinear the observation model and the evolution model are with respect to the parameters.

In the (extended) Kalman filter algorithm, the estimates $f_{t|t}$ are computed from current and past data, and thus it can be used in real-time data processing. If the data processing can be done off line, the estimates for each state can also be determined based on the whole data set $\{z_t, t = 1, \dots, T\}$. The algorithm is called the fixed-interval smoother,⁵⁹ and the estimates $f_{t|T}$ are computed from the results of extended Kalman filtering by performing a backward run ($t = T, T - 1, \dots, 2$) with equations

$$X_{t-1} = C_{t-1|t-1} K_{t-1}^T C_{t|t-1}^{-1}, \quad (26)$$

$$f_{t-1|T} = f_{t-1|t-1} + X_{t-1} (f_{t|T} - f_{t|t-1}). \quad (27)$$

There exist several different derivations and forms for the Kalman filter algorithms. These, together with a detailed exposition of the Kalman filter algorithms, can be found, for example, in Refs. 59 and 61. For the statistical (Bayesian) interpretation of Kalman filtering techniques, see Ref. 57.

We note that the state-estimation approach has previously been applied (implicitly) to the OT problem in Refs. 41 and 42. However, in those papers Kalman filtering techniques were used only to solve the stationary OT problem (i.e., choosing $K_t = I$ and $C_{w,t} = 0$ in our model).

The state-estimation approach provides regularization in the temporal direction. We note that in most cases the state-estimation approach to OT may necessitate spatial regularization because of the ill-posed nature of the OT problem. Using the idea of generalized Tikhonov regularization, one can introduce spatial regularization into the state-estimation problem by replacing the observation model (19) by an augmented equation

$$\begin{pmatrix} z_t - F_t(f_t^*) + J_t(f_t^*)f_t^* \\ 0 \end{pmatrix} = \begin{pmatrix} J_t(f_t^*) \\ \sqrt{\beta}R \end{pmatrix} f_t + \begin{pmatrix} n_t \\ \hat{n}_t \end{pmatrix}, \quad (28)$$

where $\beta > 0$ is the regularization parameter, R is the regularization operator as in Eq. (15), and \hat{n}_t denotes a fictitious noise process for the additional “observations” that are based on (spatial) *a priori* information or assumptions about the parameters. The augmentation of state-space models by spatial prior models was originally presented in Ref. 38.

4. RESULTS

A. Measurement Protocols and Initializations

In the following simulations, two different data-acquisition protocols are considered. The first one is a traditional 16×16 system, which consists of 16 source fibers and 16 detector fibers placed in equiangular positions on the exterior boundary $\partial\Omega$ of a circular body Ω that has a diameter of 50 mm. The configuration of the sources for this system is illustrated in Fig. 1(a). The second data-acquisition protocol that is considered is a 4×16 system with four source fibers and 16 detector fibers placed in equiangular positions on the boundary $\partial\Omega$ of the circular body Ω . The configuration of the sources for the 4×16 protocol is illustrated in Fig. 1(b). The motivation behind giving results with two different data-acquisition protocols is to illustrate that, in addition to a proper choice of the inversion method, the adjustment of the measurement sequence can yield further improvement to the results in the case of the nonstationary OT problem.

The data type that we use is the continuous-wave (cw) intensity; i.e., the measured quantity at the detector sites ζ_i is the transmitted intensity for a constant intensity input (source modulation frequency $\omega = 0$) at a source site ε_k . Whereas the information content of the cw data is weaker than that of the frequency-domain or time-resolved measurements, this choice was made because of the faster data acquisition in cw systems. Further, in the following simulations, the data acquisition for both protocols is carried out such that a single source is fired at time

t_i and the transmitted intensity is measured on all 16 detector locations ζ_i , $i = 1, 2, \dots, 16$ simultaneously (i.e., parallel acquisition of all the channels). Thus we have data vector $z_t = z^{(t)} \in \mathbb{R}^{16}$ at each time instant t in the state estimation. Thus, for the 16-source system, the time that is needed to measure a traditional (16×16) frame $z \in \mathbb{R}^{256}$ consists of 16 time steps, and for the four-source system the time that is needed to measure a “traditional” (4×16) frame $z \in \mathbb{R}^{64}$ consists of four time steps.

In the generation of the synthetic cw data, we discretized the object domain Ω to $N_e = 11,760$ triangular elements with a total number of $N_n = 6009$ vertex nodes. Gaussian random noise with standard deviation of 1% of the measured signal was added to the simulated data.⁶³ In the construction of the phantom domains, the values for the absorption coefficients μ_a and the (reduced) scattering coefficients μ'_s were chosen from the range of interest in medical imaging,⁸ and then the values for the diffusion coefficient were computed by using the relation $\kappa = [3(\mu_a + \mu'_s)]^{-1}$.

In the state estimation, we used a FE mesh that consisted of $N_e = 5776$ triangular elements with a total number of $N_n = 3017$ vertex nodes. The absorption and diffusion coefficients were represented in a pixel mesh that consists of 496 disjoint quadrilateral pixels. Each of these pixels is a union of several triangular FE elements. This discretization is essentially identical to the “Joshua tree” in Ref. 64.

The recovery of both absorption and diffusion coefficients based on cw data is a nonunique inverse problem.⁵⁴ Because of the nonunique nature of the cw problem, only the absorption coefficient is reconstructed in the following examples. Thus we have $f_t = \mu_a \in \mathbb{R}^{496}$. Absorption was chosen because of the fact that it is of primary interest in most medical applications (see, e.g., Refs. 65 and 66). Further, in the state-estimation computations, we make the usual assumption that diffusion coefficient is independent of absorption. Thus the initial diffusion vector κ remains unchanged in the state-estimation process. Although the above assumption is incorrect, it can usually be justified by specifying the condition $\mu_a \ll \mu'_s$.^{8,25}

For the state evolution matrix K_t , we used the trivial

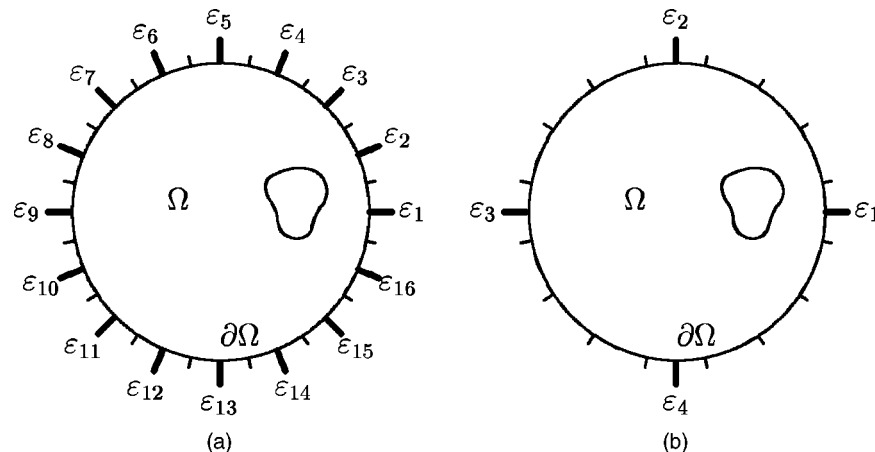


Fig. 1. Illustration of the source configurations for the data-acquisition protocols: (a) traditional 16×16 protocol, (b) 4×16 protocol. Thick tick marks denote the locations of the source fibers ε_k , and shorter thin marks denote the locations of the detector fibers. For both protocols, the indices of the sources are in accordance with the sequence in which they are fired.

time-invariant choice $K_t = I$; i.e., the state evolution model (16) becomes the 496-variate random-walk model. For the covariance matrix of the state noise process w_t , we use $C_{w,t} = C_w = \sigma_w^2 I$; i.e., we assume that the state noise process is a zero-mean Gaussian process with equal (time-invariant) variance σ_w^2 in each variable. Loosely speaking, the construction/choice of the state covariance matrix C_w can be regarded as the choice of the temporal regularization parameter and can be viewed as a close analog to the selection of the regularization parameter in Tikhonov regularization. In this study, the value of σ_w^2 was chosen by performing a set of simulations. We used the value $\sigma_w^2 = 0.001$. For discussions on more systematic ways to construct the state noise covariance matrix, see, e.g., Refs. 40 and 62.

Because of the ill-posed nature of the OT problem, we used the (spatially) regularized observation model (28). Because of the large dynamical range of OT data, the self-normalized cw data were used as data type in the state estimation.^{8,34} With this choice, the (linearized) observation model (19) assumes the form

$$Lz_t = LF_t(f_t^*) + LJ_t(f_t^*)(f_t - f_t^*) + Ln_t,$$

where $L = \text{diag}[F_t(f_t^*)^{-1}]$. For the covariance of the (scaled) observation noise Ln_t , we used (time-invariant) covariance matrix $C_{n,t} = C_n = \sigma_n^2 I$ with $\sigma_n = 0.01$. For the self-normalized data, this choice is an approximation for the noise model that was used in the simulated data. In practical systems, a feasible measurement noise covariance matrix $C_{n,t}$ can be determined by analysis and evaluation of the measurement system.^{27,63,67} As the regularization matrix R in Eq. (28), we used the Hessian of an approximate total-variation penalty functional (for details see Refs. 53 and 68). For the covariance matrix of the fictitious observation errors, we used $C_{\hat{n}_t} = I$, leading to an overall noise covariance matrix of the form

$$C_{\mathbf{n},t} = \begin{bmatrix} C_{n,t} & 0 \\ 0 & I \end{bmatrix}$$

for the combined noise processes $(n_t^T \hat{n}_t^T)^T \sim \mathcal{N}(0, C_{\mathbf{n},t})$.

B. Case 1—Single Dynamic Object on Constant Background

The results for the first test phantom are shown with both data-acquisition protocols. The reconstructions that are shown in Fig. 2 are based on the traditional 16×16 system, and the results that are shown in Fig. 3 are based on the 4×16 system. For both systems, the simulated data and the state estimates were computed for time instants t_i , $i = 1, 2, 3, \dots, 16$. The first columns in Figs. 2 and 3 display the true absorption distribution μ_a at time instants t_i , $i = 1, 3, 5, \dots, 15$. The red markers on the boundary $\partial\Omega$ of the phantom domains denote the location ε_k of the source that is illuminated at time t_i . In the phantom domains, the values of absorption and reduced scattering in the background region at each time instant are $\mu_a = 0.025 \text{ mm}^{-1}$ and $\mu_s' = 2 \text{ mm}^{-1}$, respectively, resulting in the diffusion value $\kappa = 0.1646 \text{ mm}$. For the circular inclusion, which moves in a circular path in a counterclockwise direction, the values at each time instant are $\mu_a = 0.05 \text{ mm}^{-1}$ and $\mu_s' = 4 \text{ mm}^{-1}$, resulting in

$\kappa = 0.0823 \text{ mm}$. Although this simple constant-level moving-inclusion case may be a bit unrealistic from a practical viewpoint, it serves as a good starting point for the evaluation of the proposed method.

The second columns in Figs. 2 and 3 show the (extended) Kalman filter estimates $f_{t|t}$, and the third columns show the (fixed-interval) Kalman smoother estimates $f_{t|T}$ at the same time instants. In the initialization of the state estimation, we used the values $\mu_a = 0.025 \text{ mm}^{-1}$ for the absorption [i.e., $f_{1|0} = (0.025, 0.025, \dots, 0.025)^T \in \mathbb{R}^{496}$] and $\mu_s' = 2 \text{ mm}^{-1}$ for the reduced scattering, leading to $\kappa = 0.1646 \text{ mm}$. Obviously, in the case of Figs. 2 and 3, this means that the true values of the absorption and the reduced scattering in the background were assumed to be known in the initialization. As the linearization point of the observation model in the state estimation, we used the current value of the Kalman predictor estimate at each time step; that is, we used $f_t^* = f_{t|t-1}$. The same constant diffusion vector was used (in the forward problem) throughout the computation of the results in Figs. 2 and 3. For the estimation error covariance, we used the initialization $C_{1|0} = 0.025I$. The initialization of $C_{1|0}$ is usually set relatively wide, which, loosely speaking, means that our knowledge of the parameters before any measurements is weak. If the initialization of $C_{1|0}$ is set too narrow and the initialization of $f_{1|0}$ is far from the truth, the Kalman recursions usually exhibit a long “burn-in” period before providing useful estimates. In addition, the effects of the “large” initialization $C_{1|0}$ tail off after a few time steps of the Kalman recursions. The parameter β for the spatial regularization was chosen by a set of simulations. We used the value $\beta = 1$.

The reconstructions in Figs. 2 and 3 are shown such that each column has its own color scale. The reconstructed values of absorption in the set of filter estimates $f_{t|t}$ in Fig. 2 are in the range $0.0165\text{--}0.0376 \text{ mm}^{-1}$, and for the smoother estimates $f_{t|T}$ the respective range is $0.0162\text{--}0.0376 \text{ mm}^{-1}$. In Fig. 3, the reconstructed values of absorption in the filter estimates $f_{t|t}$ are in the range $0.0113\text{--}0.0427 \text{ mm}^{-1}$, and for the smoother estimates $f_{t|T}$ the respective range is $0.0144\text{--}0.0418 \text{ mm}^{-1}$.

The fourth and fifth columns in Figs. 2 and 3 show stationary reconstructions (i.e., f is implicitly assumed to be time invariant) based on the same data that are used in the state estimation.

The reconstructions that are shown in the fourth columns of Figs. 2 and 3 are computed by using the simultaneous detector readings for the single source ε_k that is fired at time t_i (i.e., we have data vector $z \in \mathbb{R}^{16}$). The reconstructions are computed by using the Tikhonov-regularized output LS approach [Eqs. (14) and (15)]. The regularization operator R was the same as that used for the spatial regularization of the state-estimation approach. The regularization parameter β was chosen by performing a set of simulations. We used the value $\beta = 0.01$. The initialization of (μ_a, μ_s') was the same as that in the state-estimation approach. The optimization problem was solved by using the Gauss–Newton method (for details see, e.g., Refs. 8 and 53). At each time instant, essential convergence of the Gauss–Newton

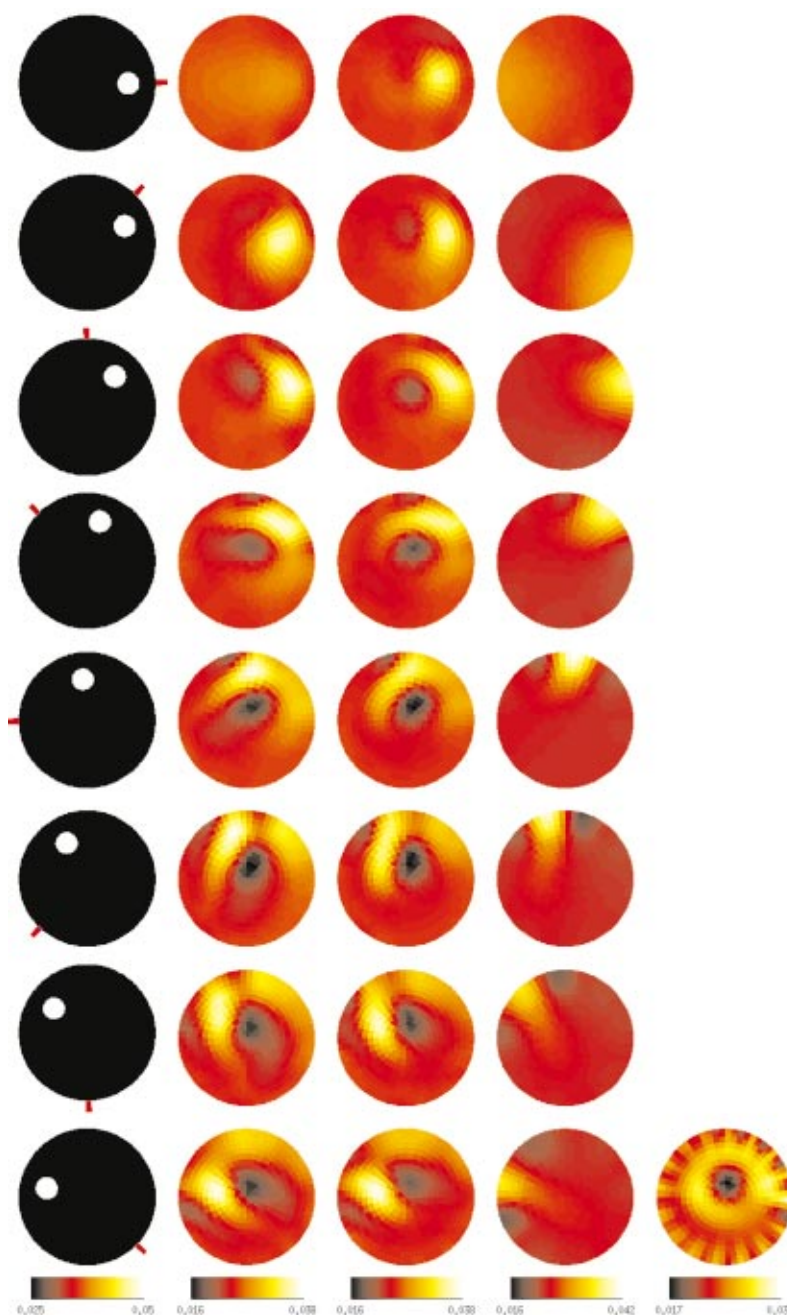


Fig. 2. True absorption images are shown in the first column at eight time instants t_i , $i = 1, 3, 5, 7, 9, 11, 13, 15$. The data-acquisition protocol was the 16×16 system. The red markers on the boundary of the phantom domains denote the source that is fired at time t_i . The Kalman filter estimates $f_{t|t}$ are shown in the second column, and the Kalman smoother estimates $f_{t|T}$ are shown in the third column. The current value of the Kalman predictor was used as linearization point of the observation model at each time instant; i.e., $f_t^* = f_{t|t-1}$. The fourth column shows stationary reconstructions that are based on the 16 detector readings for the single source that is fired at time t_i (i.e., $z \in \mathbb{R}^{16}$). The fifth column shows stationary reconstruction that is based on the traditional 16×16 frame (i.e., $z \in \mathbb{R}^{256}$) that is acquired during the instants $\{t_i, i = 1, 2, 3, \dots, 16\}$.

method was obtained in three iterations. It should be noted that the single-source data $z \in \mathbb{R}^{16}$ do not violate the stationarity assumption in this test case. Thus the stationary reconstructions in the fourth columns of Figs. 2 and 3 can be seen as an attempt to reconstruct the states by using only the spatial prior and the data $z \in \mathbb{R}^{16}$ that are obtained at each instant, without any temporal correlation between the states. The range of reconstructed absorption values for the stationary recon-

structions in the fourth column of Fig. 2 is $0.0157\text{--}0.0425 \text{ mm}^{-1}$. In Fig. 3, the corresponding range of reconstructed absorption values is $0.0160\text{--}0.0429 \text{ mm}^{-1}$.

The stationary reconstruction shown in the fifth column of Fig. 2 is based on the traditional 16×16 data frame (i.e., $z \in \mathbb{R}^{256}$) that is acquired during the time instants $\{t_i, i = 1, 2, 3, \dots, 16\}$. Obviously, this frame violates strongly the stationarity assumption of the regularized output LS approach. For this reconstruction, the

regularization parameter was $\beta=1$. Three iterations of the Gauss–Newton algorithm were computed. The range of reconstructed absorption values is $0.0170\text{--}0.0336\text{ mm}^{-1}$.

The stationary reconstructions that are shown in the fifth column of Fig. 3 are based on the 4×16 frames (i.e., $z \in \mathbb{R}^{64}$) that contain all four data vectors $z^{(t)} \in \mathbb{R}^{16}$ that are measured during the time instants t_i , $i = n, n-1, n-2, n-3$, needed to acquire data for all four

source locations of the system. For the stationary reconstructions in the fifth column of Fig. 3, the regularization parameter was $\beta = 0.1$. Reconstructions were computed for all instants $\{t_i, i = 4, 5, 6, \dots, 16\}$ for which a full 4×16 frame is available. For each time instant t_i , essential convergence of the Gauss–Newton method was obtained in three iterations. Reconstructions are shown at time instants $\{t_i, i = 5, 7, \dots, 15\}$. For the set of traditional reconstructions that are based on the 4×16

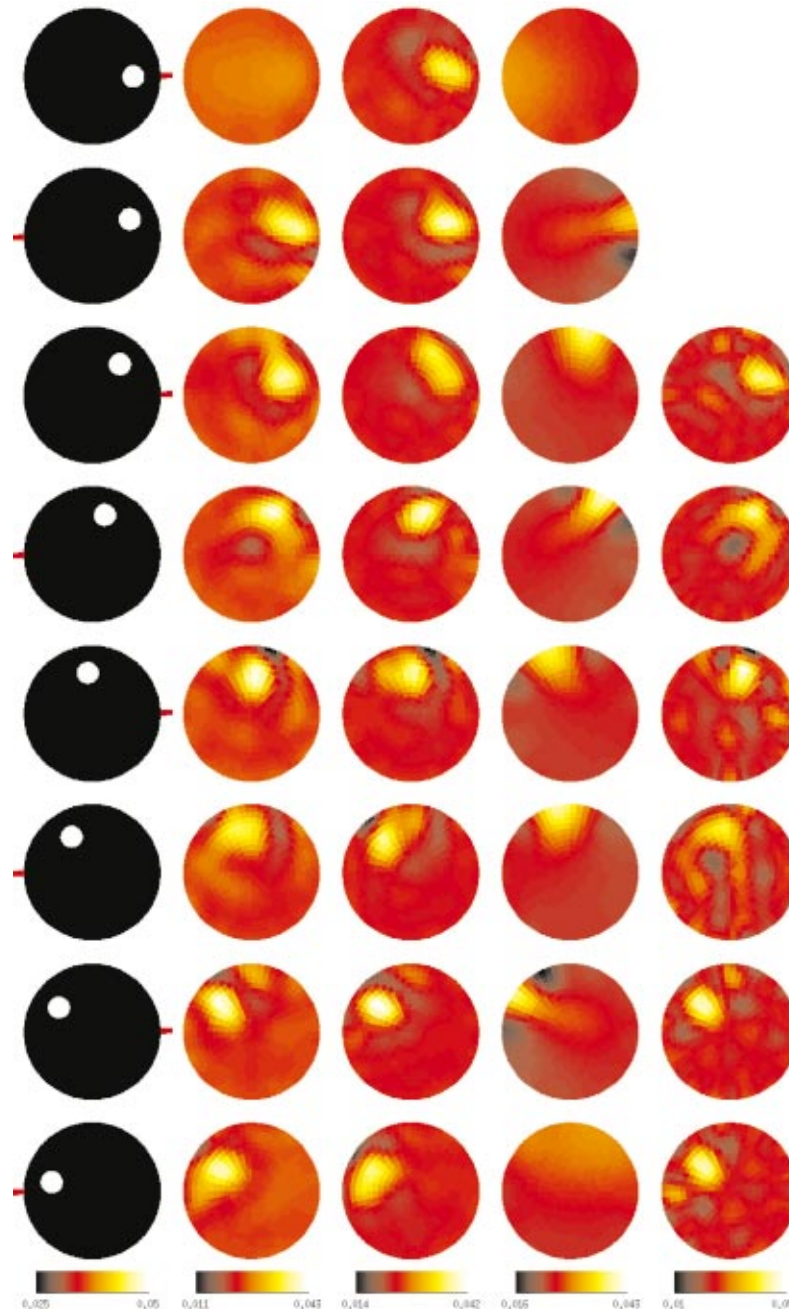


Fig. 3. True absorption images are shown in the first column at eight time instants t_i , $i = 1, 3, 5, 7, 9, 11, 13, 15$. The data-acquisition protocol was the 4×16 system. The red markers on the boundary of the phantom domains denote the source that is fired at time t_i . The Kalman filter estimates $f_{t|t}$ are shown in the second column, and the Kalman smoother estimates $f_{t|T}$ are shown in the third column. The current value of the Kalman predictor was used as linearization point of the observation model at each time instant; i.e., $f_t^* = f_{t|t-1}$. The fourth column shows (stationary) reconstructions that are based on the detector readings for the single source that is fired at time t_i (i.e., $z \in \mathbb{R}^{16}$). The fifth column shows stationary reconstructions based on the 4×16 frame (i.e., $z \in \mathbb{R}^{64}$) that is acquired during instants $\{t_{i-3}, t_{i-2}, t_{i-1}, t_i\}$.

frame, the range of reconstructed absorption values is 0.0095–0.0513 mm⁻¹.

As can be seen from the fifth column of Fig. 2, the stationary reconstruction that is based on the traditional 16 × 16 frame is useless in this relatively simple test case, whereas the state-estimation approach yields estimates in which the inclusion is localized reasonably well at each time instant. One notable feature in the state estimates is that they tend to exhibit a larger tail for the later time instants. This phenomenon can be explained by the fact that with the traditional 16 × 16 data-acquisition protocol several consecutive observation vectors $z^{(t)} \in \mathbb{R}^{16}$, which are taken for sources that are on opposite sides of Ω with respect to the inclusion, are, loosely speaking, relatively uninformative about the inclusion. In the absence of a good state evolution model, this lack of informative data for several consecutive time instants is seen as larger errors and lag in the estimates.

Further, as can be seen from the second and third columns of Fig. 3, the Kalman filter estimates $f_{t|t}$ and smoother estimates $f_{t|T}$ are improved in this test case when the 4 × 16 data-acquisition protocol is used instead of the traditional 16 × 16 system. With the 4 × 16 system, the inclusion is reconstructed and localized with good accuracy at each time instant. This difference between the results in Figs. 2 and 3 reflects the simple fact that the adjustment of the measurement sequence can lead to improved results in dynamical OT.

The stationary reconstructions that are based on the data $z \in \mathbb{R}^{16}$ for a single source (fourth columns in Figs. 2 and 3) are erroneous and much worse than the estimates obtained by the state-estimation approach. This difference can be explained by the fact that, whereas the state-estimation method uses the information of all the past and current data and the temporal correlation between the states provided by the state evolution model, the stationary method uses only the current data $z \in \mathbb{R}^{16}$, which do not alone provide sufficient information (in addition to the spatial smoothness prior) for the reconstruction of the absorption distribution. The notable feature in the fourth columns of Figs. 2 and 3 is that the image is concentrated in the boundary of the domain Ω , which is a common observation if stationary reconstruction is attempted by using only the projection from one source, and is a consequence of the greater weighting of the Jacobian rows near sources and detectors.⁶⁹ Note also that the second and fourth columns in row 1 of Fig. 3 are based on the same data but look different, because the nature of the prior for the second and fourth columns is different.

An interesting finding in Fig. 3 is that the stationary reconstructions (fifth column), which are based on the 4 × 16 frame of the four-source measurement protocol, are almost as good as the Kalman filter and smoother estimates in this simple test case. This result lends some support to the idea that the use of stationary reconstruction methods with a fast, suitably chosen data-acquisition protocol may be a feasible approach in certain dynamical OT studies.³⁷ However, we also computed results for the test phantom in Figs. 2 and 3 with temporally varying background values of μ_a and μ'_s . The absorption of the background of the simulated phantoms had ±10% (uniform) random variation around the value μ_a

= 0.025 mm⁻¹, and the scattering of the background had 5% variation around $\mu'_s = 2$ mm⁻¹ between the time instants t_i . Whereas the Kalman filter and smoother estimates for the test case with randomly varying background were almost as good as the ones shown in Figs. 2 and 3, the stationary reconstructions based on the 4 × 16 frames were considerably degraded compared with those shown in the fifth column of Fig. 3. The degradation of the stationary reconstructions was especially seen as large errors close to the sources. These errors were due to the variation of the background absorption and scattering during the time that is needed to acquire the 4 × 16 frame.

C. Case 2—Two Inclusions with Independent Dynamics

Results for the second test case are shown in Fig. 4. Results are shown only for the 4 × 16 data-acquisition protocol. The cross section of the phantom domains at time instants $\{t_i, i = 1, 3, \dots, 15\}$ are shown in the first column. In this test case, the domain Ω contained two inclusions with different dynamics. The background values for μ_a and μ'_s in the phantom domain at each instant are as in Fig. 3, that is, $\mu_a = 0.025$ mm⁻¹ and $\mu'_s = 2$ mm⁻¹, resulting in a diffusion value $\kappa = 0.1646$ mm. For the circular inclusion, which moves in a circular path in a clockwise direction, the values at each time instant are $\mu_a = 0.05$ mm⁻¹ and $\mu'_s = 4$ mm⁻¹, resulting in $\kappa = 0.0823$ mm. For the second inclusion, which moves radially downward, the respective values are $\mu_a = 0.05$ mm⁻¹ and $\mu'_s = 2$ mm⁻¹, resulting in $\kappa = 0.1626$ mm.

The second column in Fig. 4 shows the (extended) Kalman filter estimates $f_{t|t}$, and the third column shows the (fixed-interval) Kalman smoother estimates $f_{t|T}$ at the same time instants. All the parameters and initializations of the state estimation were the same as those used in Figs. 2 and 3; that is, we used $\mu_a = 0.025$ mm⁻¹ [i.e., $f_{1|0} = (0.025, 0.025, \dots, 0.025)^T \in \mathbb{R}^{496}$], $C_{1|0} = 0.025I$, and $\beta = 1$. For the reduced scattering, we used $\mu'_s = 2$ mm⁻¹, leading to $\kappa = 0.1646$ mm. The same constant diffusion value was used in the forward problem throughout the computation of the results in Fig. 4. The range of reconstructed absorption values is 0.0191–0.0320 mm⁻¹ for the filter estimates and 0.0197–0.0315 mm⁻¹ for the smoother estimates.

The stationary estimates that are based on the simultaneous detector readings for the single source ε_k that is fired at time t_i (i.e., $z \in \mathbb{R}^{16}$) are shown in the fourth column of Fig. 4, and the stationary estimates that are based on the 4 × 16 frame (i.e., $z \in \mathbb{R}^{64}$) are shown in the fifth column of Fig. 4. The latter estimates are shown at time instants $\{t_i, i = 5, 7, \dots, 15\}$. The initializations of (μ_a, μ'_s) and the values of regularization parameter β were the same as those for Fig. 3. For each time instant, three iterations of the Gauss–Newton algorithm were computed for both stationary reconstructions. The range of reconstructed absorption values for the stationary reconstructions in the fourth column is 0.0206–0.0326 mm⁻¹, and in the fifth column the respective range is 0.0152–0.0346 mm⁻¹.

As can be seen, the state-estimation approach also yields reasonably good results in this more complex case

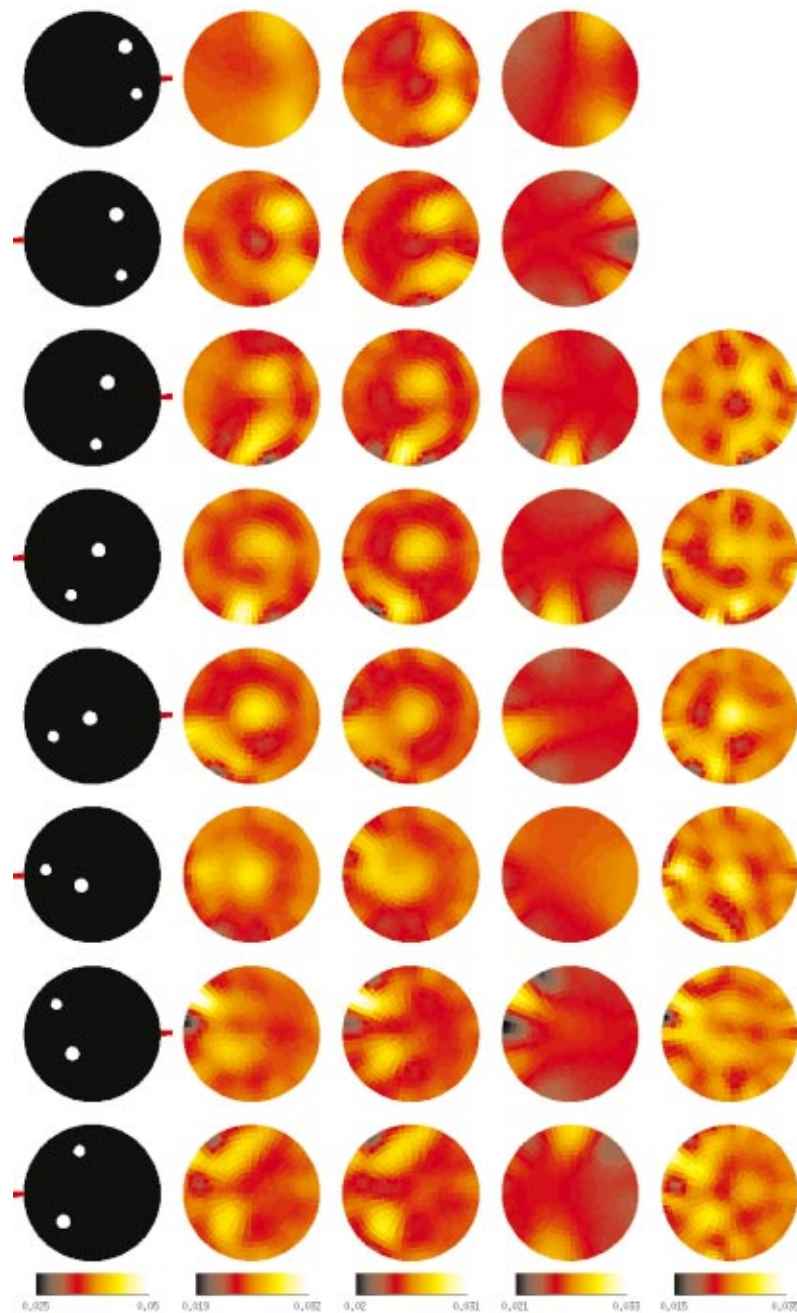


Fig. 4. True absorption images are shown in the first column at eight time instants t_i , $i = 1, 3, 5, 7, 9, 11, 13, 15$. The data-acquisition protocol was the 4×16 system. The red markers on the boundary of the phantom domains denote the source that is fired at time t_i . The Kalman filter estimates $f_{i|t}$ are shown in the second column, and the Kalman smoother estimates $f_{i|T}$ are shown in the third column. The current value of the Kalman predictor was used as linearization point of the observation model at each time instant, i.e., $f_i^* = f_{i|t-1}$. The fourth column shows (stationary) reconstructions that are based on the detector readings for the single source that is fired at time t_i (i.e., $z \in \mathbb{R}^{16}$). The fifth column shows (stationary) reconstructions that are based on the traditional 4×16 frame (i.e., $z \in \mathbb{R}^{64}$) that is acquired during instants $\{t_{i-3}, t_{i-2}, t_{i-1}, t_i\}$.

with two moving inclusions. Both of the inclusions are distinguishable at almost every instant, and the localization of the inclusions is relatively accurate. Further, the advantage of the state-estimation approach over the stationary method is more evident in this test case. The stationary reconstructions in the fourth and fifth columns of Fig. 4 exhibit artifacts and mislocalization of the inclusions at most time instants. Kalman filter and smoother estimates were also computed with the 16×16 data-

acquisition protocol. The 4×16 protocol also provided better results in this more complex test case.

D. Case 3—Inclusion with Time-Varying Contrast

Results for the third test case are shown in Figs. 5 and 6. Results are shown only for the 4×16 data-acquisition protocol. In this test case, the phantom domain consists of a single fixed-position inclusion with time-varying ab-

sorption contrast. The values of μ_a and μ'_s in the background at each instant are $\mu_a = 0.025 \text{ mm}^{-1}$ and $\mu'_s = 1 \text{ mm}^{-1}$, leading to diffusion value $\kappa = 0.3252 \text{ mm}$. The value of scattering within the inclusion is the same as that in the background but absorption within the inclusion is varying sinusoidally in the range $0.025\text{--}0.045 \text{ mm}^{-1}$, leading to diffusion values in the range $\kappa = 0.3190$ to 0.3252 mm . The phantom domain at time instants $\{t_i, i = 5, 6, 7, 8\}$ are shown in the first column of Fig. 5. The sinusoidally varying value of absorption within the inclusion is shown as the thick solid curve in Fig. 6.

The second column of Fig. 5 shows the (extended) Kalman filter estimates $f_{t|t}$, and the third column shows the (fixed-interval) Kalman smoother estimates $f_{t|T}$ at the same time instants. The initialization of the state estimation was the same as that used in Subsection 4.B; that is, we used $f_{1|0} = (0.025, 0.025, \dots, 0.025)^T \in \mathbb{R}^{496}$ and $C_{1|0} = 0.025I$. For reduced scattering, we used the constant value $\mu'_s = 1 \text{ mm}^{-1}$, leading to $\kappa = 0.3252 \text{ mm}$. The same constant diffusion value was used in the forward problem throughout the computation of the results in Figs. 5 and 6. For the spatial regularization parameter, we used the value $\beta = 0.01$. The range of reconstructed absorption values for the filter estimates in the whole domain Ω is $0.0185\text{--}0.0348 \text{ mm}^{-1}$, and for the smoother estimates it is $0.0203\text{--}0.0348 \text{ mm}^{-1}$. Further, the mean value of reconstructed absorption within the in-

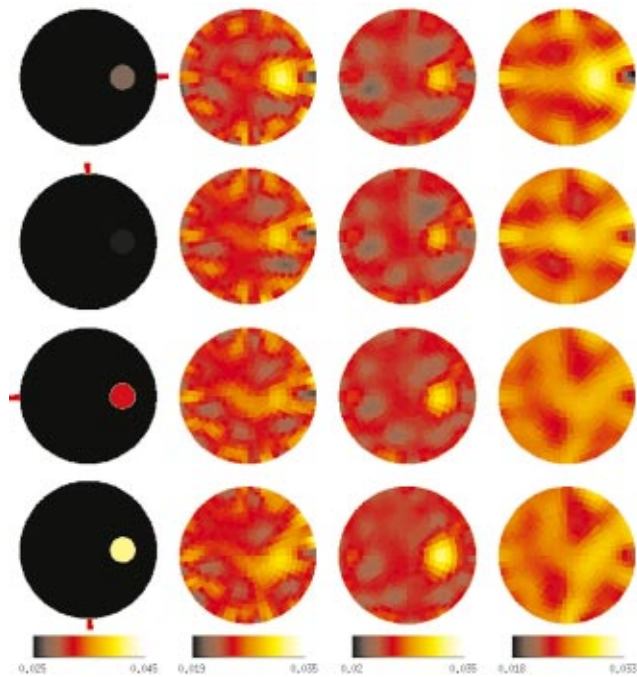


Fig. 5. True absorption images are shown in the first column at four consecutive time instants t_i , $i = 5, 6, 7, 8$. The data-acquisition protocol was the 4×16 system. The red markers on the boundary of the phantom domains denote the source that is fired at time t_i . The Kalman filter estimates $f_{t|t}$ are shown in the second column, and the Kalman smoother estimates $f_{t|T}$ are shown in the third column. The current value of the Kalman predictor was used as linearization point of the observation model at each time instant; i.e., $f_i^* = f_{t|t-1}$. The fourth column shows (stationary) reconstructions that are based on the traditional 4×16 frame (i.e., $z \in \mathbb{R}^{64}$) that is acquired during instants $\{t_{i-3}, t_{i-2}, t_{i-1}, t_i\}$.

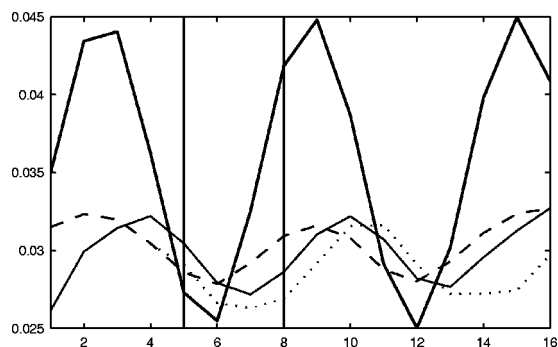


Fig. 6. Time-varying contrast of absorption within the inclusion in Fig. 5 at time instants t_i , $i = 1, 2, \dots, 16$. The true value is shown as the thick solid curve. The mean value of the reconstructed absorption within the inclusion for the Kalman filter estimates $f_{t|t}$ is shown as the thin solid curve and for the Kalman smoother estimates $f_{t|T}$ is shown as the dashed curve. The dotted curve shows the respective value for the stationary reconstructions with the 4×16 frame (i.e., $z \in \mathbb{R}^{64}$) at time instants t_i , $i = 4, 5, \dots, 16$. The vertical lines denote the part of the time series that is shown in Fig. 5.

clusion for the Kalman filter (thin solid curve) and smoother (dashed curve) estimates are shown in Fig. 6.

Stationary estimates that are based on the 4×16 frames (i.e., $z \in \mathbb{R}^{64}$) at time instants $\{t_i, i = 5, 6, 7, 8\}$ are shown in the fourth column of Fig. 5. The range of reconstructed absorption values for the stationary estimates in the whole domain Ω is $0.0176\text{--}0.0327 \text{ mm}^{-1}$. The mean value of the reconstructed absorption within the inclusion is shown as the dotted curve in Fig. 6. The initialization of (μ_a, μ'_s) in the Gauss–Newton algorithm was the same as that used in the state estimation. The value of the regularization parameter was $\beta=0.1$, and the number of Gauss–Newton iterations was 3.

Stationary reconstructions that are based on data for a single source (i.e., $z \in \mathbb{R}^{16}$) were erroneous also in this time-varying contrast test case. Qualitatively, they were similar to those in Figs. 3 and 4. These were left out of Figs. 5 and 6.

As can be seen from Figs. 5 and 6, the state-estimation approach yields relatively good results in this varying-contrast case. The temporal trend of the time-varying contrast within the inclusion is reconstructed well in a qualitative sense. Whereas the Kalman filter estimates (thin solid curve in Fig. 6) exhibit a short delay, the temporal trend of the absorption contrast is found with good accuracy with the Kalman smoother estimates (dashed curve). Also, it is evident from Figs. 5 and 6 that the stationary reconstructions that use data from four time instants exhibit more errors and lag than those from the state-estimation approach. The quantitative values of the absorption contrast are not found accurately. This can be expected as a result of nonlinearity and the ill-posed nature of the problem. In this test case, the Kalman filter and smoother estimates with the 16×6 data-acquisition protocol were almost as good as those with the 4×16 protocol.

5. DISCUSSION

In this paper, we proposed a new numerical approach to the nonstationary OT problem. The assumption in the

method is that the absorption and/or diffusion coefficients may exhibit significant changes during the acquisition of data for one traditional image frame. In the proposed method, the OT inverse problem is formulated as a state-estimation problem in which the objective is to compute state estimates for the coefficients at each time instant, given the observations and the state evolution and observation models. In this study, the state estimates were computed by using the extended Kalman filter and the fixed-interval smoother. The performance of the method was evaluated by using synthetic cw data.

The state-estimation approach allows natural and systematic use of temporal prior information about the time-varying optical coefficients through the state evolution model. In this study, we used the most trivial model, namely, the random-walk model, as the state evolution model. Although this simple model, which was chosen *ad hoc*, was not a particularly suitable choice for the moving-inclusion and sinusoidally varying contrast cases considered here, the proposed approach gave relatively good results. Also, the state-estimation approach gave better results than the traditional stationary reconstruction method. Based on these initial results, the performance of the state-estimation approach in dynamical OT studies seems promising. To utilize fully the potential of the state-estimation approach, work has to be done on the development of more appropriate, application-specific state evolution models for different applications of dynamical OT. Arguably, a significant improvement to the results can be obtained if a feasible state evolution model, which is based on assumed/known temporal properties of the target, is available. In medical applications, the state evolution model can be based on, for example, physical models of blood flow or properties of physiological signals such as heart rate, and in industrial applications it can be based on flow models in process pipelines. Such models have been considered previously in Ref. 39, in which a stochastic convection-diffusion-type evolution model was applied to the dynamical electrical impedance tomography problem in a process tomography application.

In this study, two different measurement systems were considered. The first one was the traditional 16×16 system, and the second one was a 4×16 system. In the test cases considered here, the four-source system provided better results than the traditional 16-source system. However, these results should not be interpreted as indicating that the four-source system, which was chosen here more or less *ad hoc*, would be an optimal data-acquisition protocol for any given situation: The motivation for using two different protocols was just to illustrate that the adjustment of the measurement protocol can lead to further improvements in nonstationary cases. The development of optimal measurement sequences for different applications of dynamical OT is an important topic for future work.

In this study, we restricted ourselves to simulations using a two-dimensional model, cw data, and absorption-only reconstructions. In principle, the method is directly applicable to three-dimensional OT and to other measurement types such as frequency- or time-domain data. However, three-dimensional OT is a computationally very demanding problem. Progress in stationary three-

dimensional imaging has been reported previously in, for example, Refs. 70–72. One topic for future work is the development of efficient computational schemes for the application of the state-estimation approach to three-dimensional OT. Also, evaluation using measured data is a topic for future studies, where we hope also to include measured estimates of the data noise covariance statistics.

ACKNOWLEDGMENTS

This work was supported by National Technology Agency of Finland (TEKES) contract 40781/00 and the Saastamoinen foundation. S. R. Arridge acknowledges the Wellcome Trust for an international Biomedical Research Collaboration grant. S. Prince acknowledges the Engineering and Physical Sciences Research Council for support of a Research Masters program.

Corresponding author Simon R. Arridge may be reached by e-mail at S.Arridge@cs.ucl.ac.uk.

REFERENCES

1. M. Cutler, "Transillumination as an aid in the diagnosis of breast lesions," *Surg. Gynecol. Obstet.* **48**, 721–729 (1929).
2. J. J. Jöbsis, "Noninvasive infrared monitoring of cerebral and myocardial oxygen sufficiency and circulatory parameters," *Science* **198**, 1264–1267 (1977).
3. G. Jarry, S. Ghesquiere, J. M. Maarek, S. Debray, Bui-Mong-Hung, and D. Laurent, "Imaging mammalian tissues and organs using laser collimated transillumination," *J. Biomed. Eng.* **6**, 70–74 (1984).
4. S. R. Arridge, "The forward and inverse problems in time-resolved infrared imaging," in *Medical Optical Tomography: Functional Imaging and Monitoring*, G. J. Mueller, B. Chance, R. R. Alfano, S. R. Arridge, J. Beuthan, E. Gratton, M. Kaschke, B. R. Masters, S. Svanberg, and P. van der Zee, eds., Vol. IS11 of SPIE, Institute Series (Society of Photo-Optical Instrumentation Engineers, Bellingham, Wash., 1993), pp. 35–64.
5. A. Yodh and B. Chance, "Spectroscopy and imaging with diffusing light," *Phys. Today* **48**, 38–40 (1995).
6. J. C. Hebden, S. R. Arridge, and D. T. Delpy, "Optical imaging in medicine: I. Experimental techniques," *Phys. Med. Biol.* **42**, 825–840 (1997).
7. S. R. Arridge and J. C. Hebden, "Optical imaging in medicine: II. Modelling and reconstruction," *Phys. Med. Biol.* **42**, 841–853 (1997).
8. S. R. Arridge, "Optical tomography in medical imaging," *Inverse Probl.* **15**, R41–R93 (1999).
9. D. Hawysz and E. M. Sevick-Muraca, "Developments towards diagnostic breast cancer imaging using near-infrared optical measurements and fluorescent contrast agents," *Neoplasia* **2**, 388–417 (2000).
10. D. A. Boas, D. H. Brooks, E. L. Miller, C. A. DiMarzio, M. Kilmer, R. J. Gaudette, and Q. Zhang, "Imaging the body with diffuse optical tomography," *IEEE Signal Process. Mag.* **18**, 57–75 (2001).
11. S. Fantini, M. A. Franceschini, G. Gaida, E. Gratton, H. Jess, W. W. Mantulin, K. T. Moesta, P. M. Schlag, and M. Kaschke, "Frequency-domain optical mammography: edge effect corrections," *Med. Phys.* **23**, 149–157 (1996).
12. K. T. Moesta, S. Fantini, H. Jess, S. Totkas, M. A. Franceschini, M. Kaschke, and P. M. Schlag, "Contrast features of

- breast cancer in frequency-domain laser scanning mam-mography," *J. Biomed. Opt.* **3**, 129–136 (1998).
13. H. Jess, H. Erdl, K. T. Moesta, S. Fantini, M. A. Franceschini, and E. Gratton, "Intensity modulated breast imaging: technology and clinical pilot study results," in *Advances in Optical Imaging and Photon Migration*, R. R. Alfano and J. G. Fujimoto, eds., Vol. 2 of OSA Trends in Optics and Photonics Series (Optical Society of America, Washington, D.C., 1996), pp. 126–129.
 14. S. R. Arridge and M. Schweiger, "A general framework for iterative reconstruction algorithms in optical tomography, using a finite element method," in *Computational Radiology and Imaging: Therapy and Diagnosis*, C. Borgers and F. Natteres, eds., Vol. 110 of IMA Volumes in Mathematics and Its Applications (Springer-Verlag, Berlin, 1998), pp. 45–70.
 15. J. P. van Houten, D. A. Benaron, S. Splilman, and D. K. Stevenson, "Imaging brain injury using time-resolved near infrared light scanning," *Pediatr. Res.* **39**, 470–476 (1996).
 16. J. S. Wyatt, M. Cope, D. T. Delpy, C. E. Richardson, A. D. Edwards, S. C. Wray, and E. O. R. Reynolds, "Quantitation of cerebral blood volume in newborn infants by near infrared spectroscopy," *J. Appl. Physiol.* **68**, 1086–1091 (1990).
 17. A. Villringer and B. Chance, "Non-invasive optical spectroscopy and imaging of human brain function," *Trends Neurosci.* **20**, 435–442 (1997).
 18. C. Hirth, H. Obrig, K. Villringer, A. Thiel, J. Bernarding, W. Muhlnickel, H. Flor, U. Dirnagl, and A. Villringer, "Non-invasive functional mapping of the human motor cortex using near-infrared spectroscopy," *Neuro. Report* **7**, 1977–1981 (1996).
 19. R. Wenzel, H. Obrig, J. Ruben, K. Villringer, A. Thiel, J. Bernarding, U. Dirnagl, and A. Villringer, "Cerebral blood oxygenation changes induced by visual stimulation humans," *J. Biomed. Opt.* **1**, 399–404 (1996).
 20. K. R. Heercken, H. Obrig, R. Wenzel, K. Eberle, J. Ruben, K. Villringer, R. Kurth, and A. Villringer, "Cerebral haemoglobin oxygenation during sustained visual stimulation—a near-infrared spectroscopy study," *Philos. Trans. R. Soc. London Ser. B* **352**, 743–750 (1997).
 21. A. Kienle, L. Lilge, M. S. Patterson, R. Hibst, R. Steiner, and B. C. Wilson, "Spatially resolved absolute diffuse reflectance measurements for noninvasive determination of the optical scattering and absorption coefficients of biological tissue," *Appl. Opt.* **35**, 2304–2314 (1996).
 22. M. Kohl, R. Watson, and M. Cope, "Determination of absorption-coefficients in highly scattering media from changes in attenuation and phase," *Opt. Lett.* **21**, 1519–1521 (1996).
 23. B. Chance, J. S. Leigh, H. Miyake, D. S. Smith, S. Nioka, R. Greenfield, M. Finander, K. Kaufman, W. Levy, M. Young, P. Cohn, H. Yoshioka, and R. Boretsky, "Comparison of time-resolved and unresolved measurements of deoxyhemoglobin in brain," *Proc. Natl. Acad. Sci. USA* **85**, 4971–4975 (1988).
 24. R. A. Williams and M. S. Beck, eds., *Process Tomography, Principles, Techniques and Applications* (Butterworth-Heinemann, Oxford, UK, 1995).
 25. H. Jiang, K. D. Paulsen, U. L. Osterberg, B. W. Pogue, and M. S. Patterson, "Optical image reconstruction using frequency-domain data: simulations and experiments," *J. Opt. Soc. Am. A* **13**, 253–266 (1995).
 26. A. H. Hielscher, A. D. Klose, and K. M. Hanson, "Gradient-based iterative image reconstruction scheme for time-resolved optical tomography," *IEEE Trans. Med. Imaging* **18**, 262–271 (1999).
 27. J. C. Ye, K. J. Webb, C. A. Bouman, and R. P. Millane, "Optical diffusion tomography by iterative coordinate-descent optimization in a Bayesian framework," *J. Opt. Soc. Am. A* **16**, 2400–2412 (1999).
 28. R. J. Gaudette, D. H. Brooks, C. A. DiMarzio, M. E. Kilmer, E. L. Miller, T. Gaudette, and D. A. Boas, "A comparison study of linear reconstruction techniques for diffuse optical tomographic imaging of absorption coefficient," *Phys. Med. Biol.* **45**, 1051–1070 (2000).
 29. J. Chang, H. L. Graber, R. L. Barbour, and R. Aronson, "Recovery of optical cross-section perturbations in dense-scattering media by transport theory based imaging operators and steady state simulated data," *Appl. Opt.* **35**, 3963–3978 (1996).
 30. B. B. Das, J. Dolne, R. L. Barbour, H. L. Graber, J. Chang, M. Zavallos, F. Liu, and R. R. Alfano, "Analysis of time-resolved data for tomographical image reconstruction of opaque phantoms and finite absorbers in diffusive media," in *Optical Tomography, Photon Migration, and Spectroscopy of Tissue and Model Media: Theory, Human Studies, and Instrumentation*, B. Chance and R. R. Alfano, eds., Proc. SPIE **2389**, 16–28 (1995).
 31. M. A. O'Leary, D. A. Boas, B. Chance, and A. G. Yodh, "Experimental images of heterogeneous turbid media by frequency-domain diffusing-photon tomography," *Opt. Lett.* **20**, 426–428 (1995).
 32. J. Chang, H. L. Graber, P. C. Koo, R. Aronson, S. S. Barbour, and R. L. Barbour, "Optical imaging of anatomical maps derived from magnetic resonance images using time-independent optical sources," *IEEE Trans. Med. Imaging* **16**, 68–77 (1997).
 33. K. D. Paulsen and H. Jiang, "Enhanced frequency-domain optical image reconstruction in tissues through total variation minimization," *Appl. Opt.* **35**, 3447–3458 (1996).
 34. M. Schweiger and S. R. Arridge, "Application of temporal filters to time resolved data in optical tomography," *Phys. Med. Biol.* **44**, 1699–1717 (1999).
 35. V. Kolehmainen, M. Vauhkonen, J. P. Kaipio, and S. R. Arridge, "Recovery of piecewise constant coefficients in optical diffusion tomography," *Opt. Express* **7**, 468–480 (2000); <http://www.opticsexpress.org>.
 36. A. V. Bluestone, G. Abdoulaev, C. H. Schmitz, R. L. Barbour, and A. H. Hielscher, "Three-dimensional optical tomography of hemodynamics in the human head," *Opt. Express* **9**, 272–286 (2001); <http://www.opticsexpress.org>.
 37. C. H. Schmitz, H. L. Graber, H. Lou, I. Arif, J. Ira, Y. Pei, A. Bluestone, S. Zhong, R. Andronica, I. Soller, N. Ramirez, D.-L. S. Barbour, and R. L. Barbour, "Instrumentation and calibration protocol for imaging dynamic features in dense-scattering media by optical tomography," *Appl. Opt.* **39**, 6466–6485 (2000).
 38. J. P. Kaipio and E. Somersalo, "Nonstationary inverse problems and state estimation," *J. Inverse Ill-Posed Probl.* **7**, 273–282 (1999).
 39. A. Seppänen, M. Vauhkonen, P. J. Vauhkonen, E. Somersalo, and J. P. Kaipio, "State estimation with fluid dynamical evolution models in process tomography—an application to impedance tomography," *Inverse Probl.* **17**, 467–484 (2001).
 40. V. Kolehmainen, A. Voutilainen, and J. P. Kaipio, "Estimation of non-stationary region boundaries in EIT—state estimation approach," *Inverse Probl.* **17**, 1937–1956 (2001).
 41. M. J. Eppstein, D. E. Dougherty, T. L. Troy, and E. M. Sevick-Muraca, "Biomedical optical tomography using dynamic parameterization and Bayesian conditioning on photon migration measurements," *Appl. Opt.* **38**, 2138–2150 (1999).
 42. M. J. Eppstein, D. E. Dougherty, D. J. Hawysz, and E. M. Sevick-Muraca, "Three-dimensional Bayesian optical image reconstruction with domain decomposition," *IEEE Trans. Med. Imaging* **20**, 147–163 (2001).
 43. S. R. Arridge, M. Schweiger, M. Hiraoka, and D. T. Delpy, "A finite element approach for modeling photon transport in tissue," *Med. Phys.* **20**, 299–309 (1993).
 44. J. P. Kaltenbach and M. Kaschke, "Frequency- and time-domain modelling of light transport in random media," in *Medical Optical Tomography: Functional Imaging and Monitoring*, G. J. Mueller, B. Chance, R. R. Alfano, S. R. Arridge, J. Beuthan, E. Gratton, M. Kaschke, B. R. Masters, S. Svanberg, and P. van der Zee, eds., Vol. IS11 of SPIE Institute Series (Society at Photo-Optical Instrumentation Engineers, Bellingham, Wash., 1993), pp. 65–86.
 45. M. C. Case and P. F. Zweifel, *Linear Transport Theory* (Addison-Wesley, New York, 1967).
 46. O. Dorn, "A transport-backtransport method for optical tomography," *Inverse Probl.* **14**, 1107–1130 (1998).

47. M. Schweiger, S. R. Arridge, M. Hiraoka, and D. T. Delpy, "The finite element model for the propagation of light in scattering media: boundary and source conditions," *Med. Phys.* **22**, 1779–1792 (1995).
48. A. Ishimaru, *Wave Propagation and Scattering in Random Media* (Academic, New York, 1978), Vol. 1.
49. R. Aronson, "Boundary conditions for diffusion of light," *J. Opt. Soc. Am. A* **12**, 2532–2539 (1995).
50. F. Martelli, D. Contini, A. Taddeucci, and G. Zaccanti, "Photon migration through a turbid slab described by a model based on diffusion approximation. 2. Comparison with Monte Carlo results," *Appl. Opt.* **36**, 4600–4612 (1997).
51. A. H. Hielscher, R. E. Alcouffe, and R. L. Barbour, "Comparison of finite difference transport and diffusion calculations for photon migration in homogeneous and heterogeneous tissues," *Phys. Med. Biol.* **43**, 1285–1302 (1998).
52. S. R. Arridge, H. Dehghani, M. Schweiger, and E. Okada, "The finite element model for the propagation of light in scattering media: a direct method for domains with non-scattering regions," *Med. Phys.* **27**, 252–264 (2000).
53. V. Kolehmainen, "Novel approaches to image reconstruction in diffusion tomography," Ph.D. thesis (University of Kuopio, Kuopio, Finland, 2001); <http://venda.uku.fi/~vkolehma/>.
54. S. R. Arridge and W. R. B. Lionheart, "Non-uniqueness in diffusion-based optical tomography," *Opt. Lett.* **23**, 882–884 (1998).
55. B. W. Pogue, T. O. McBride, J. Prewitt, U. L. Östeberg, and K. D. Paulsen, "Spatially variant regularization improves diffuse optical tomography," *Appl. Opt.* **38**, 2950–2960 (1999).
56. R. E. Kalman and R. S. Bucy, "New results in linear filtering and prediction theory," *Trans. ASME J. Basic Eng.* **83**, 95–108 (1961).
57. J. L. Melsa and D. L. Cohn, *Decision and Estimation Theory* (McGraw-Hill, New York, 1978).
58. C. K. Chui and G. Chen, *Kalman Filtering with Practical Applications* (Springer-Verlag, Berlin, 1987).
59. B. D. O. Anderson and J. B. Moore, *Optimal Filtering* (Prentice-Hall, Englewood Cliffs, N.J., 1979).
60. H. W. Sorenson, ed., *Kalman Filtering: Theory and Applications* (IEEE Press, Piscataway, N.J., 1985).
61. A. Gelb, ed., *Applied Optimal Estimation* (MIT Press, Cambridge, Mass., 1974).
62. A. Seppänen, M. Vauhkonen, E. Somersalo, and J. P. Kaipio, "State space models in process tomography—approximation of state noise covariance," *Inverse Probl. Eng.* **9**, 561–585 (2001).
63. S. R. Arridge, M. Hiraoka, and M. Schweiger, "Statistical basis for the determination of optical pathlength in tissue," *Phys. Med. Biol.* **40**, 1539–1558 (1995).
64. M. Cheney, D. Isaacson, J. C. Newell, S. Simske, and J. Goble, "NOSER: an algorithm for solving the inverse conductivity problem," *Int. J. Imaging Syst. Technol.* **2**, 66–75 (1990).
65. J. E. Brazy, D. V. Lewis, M. H. Mitnick, and F. F. Jöbsis van der Vliet, "Noninvasive monitoring of cerebral oxygenation in preterm infants: preliminary observations," *Pediatrics* **75**, 217–225 (1985).
66. D. T. Delpy and M. Cope, "Quantitation in tissue near infrared spectroscopy," *Philos. Trans. R. Soc. London Ser. B* **352**, 649–659 (1997).
67. S. R. Arridge, M. Hiraoka, and M. Schweiger, "Modeling of noise for near-infrared transillumination imaging," in *Optical Tomography, Photon Migration, and Spectroscopy of Tissue and Model Media: Theory, Human Studies, and Instrumentation*, B. Chance and R. R. Alfano, eds., *Proc. SPIE* **2389**, 389–399 (1995).
68. J. P. Kaipio, V. Kolehmainen, E. Somersalo, and M. Vauhkonen, "Statistical inversion and Monte Carlo sampling methods in electrical impedance tomography," *Inverse Probl.* **16**, 1487–1522 (2000).
69. S. R. Arridge, "Photon measurement density functions. Part 1: analytical forms," *Appl. Opt.* **34**, 7395–7409 (1995).
70. S. R. Arridge, J. C. Hebden, M. Schweiger, F. E. W. Schmidt, M. E. Fry, E. M. C. Hillman, H. Dehghani, and D. T. Delpy, "A method for three-dimensional time-resolved optical tomography," *Int. J. Imaging Syst. Technol.* **11**, 2–11 (2000).
71. F. E. W. Schmidt, J. C. Hebden, E. M. C. Hillman, M. E. Fry, M. Schweiger, H. Dehghani, D. T. Delpy, and S. R. Arridge, "Multiple-slice imaging of a tissue-equivalent phantom by use of time-resolved optical tomography," *Appl. Opt.* **39**, 3380–3387 (2000).
72. J. Riley, M. Schweiger, S. R. Arridge, J. Ripoll, and M. Nieto-Vesperinas, "3D optical tomography in the presence of void regions," *Opt. Express* **7**, 462–467 (2000); <http://www.opticsexpress.org>.